Nonuniform Arrangement of Emitter-Receiver Pairs Arrangement and Compact Ultrasonic Tomography Setup

Mayank Goswami, Prabhat Munshi, Ashok Khanna, and Anupam Saxena

Abstract—Arrangements of emitter-receiver pairs with two possibilities: 1) nonuniform and 2) uniform locations, are studied. Ultrasonic computerized tomographic (UCT) setups are developed with these configurations for parallel and fan beam scanning modes. Optimization is used to determine the best nonuniform arrangement. The CT reconstructions with nonuniform emitter-receiver pair arrangements from the data acquired via computer generated pixel images and real world specimens show promising results compared with their uniform arrangement. A flow channel, e.g., a metal pipe with small ratio of pipe diameter to emitter/receiver aperture, imposes restriction on the number of emitter-receiver pairs. A practical application, for void-fraction estimation for water-air flow, is investigated with the best design. Reconstructed flow profiles and estimated air fractions match with 3-D numerical simulation obtained using FLUENT 14. Cost of a focused acoustic emitter/receiver pair and its noise response depends on its focal length. The optimized nonuniform design can be best suited for emitter/receiver pairs of small focal lengths and can aid in developing low budget and compact UCT scanners.

Index Terms—Sensor arrays, computerized tomography, design for experiments, design optimization.

I. INTRODUCTION

ULTRASOUND modality offers one of the best choices (economical, safe and compact) for emitter-receiver pair arrangements and associated circuitry to develop a low budget, small scale, and compact computerized tomography (CT) setup. Ultrasound computerized tomography (UCT) has also been a preferred modality for various industrial applications such as non-invasive fluid-flow analysis/probing [1]–[3]. Practical constraints, prior to design and development of an industrial setup, sometimes may not allow using sufficient number of emitter-receiver pairs [4]–[6]. For example,

M. Goswami is with the Nuclear Engineering and Technology Program, Indian Institute of Technology Kanpur, Kanpur 208016, India (e-mail: mayan@iitk.ac.in).

P. Munshi is with the Nuclear Engineering and Technology Program, Indian Institute of Technology Kanpur, Kanpur 208016, India, and also with the Department of Mechanical Engineering, Indian Institute of Technology Kanpur, Kanpur 208016, India (e-mail: pmunshi@iitk.ac.in).

A. Khanna is with the Department of Chemical Engineering, Indian Institute of Technology Kanpur, Kanpur 208016, India (e-mail: akhanna@iitk.ac.in).

A. Saxena is with the Department of Mechanical Engineering, Indian Institute of Technology Kanpur, Kanpur 208016, India (e-mail: anupams@iitk.ac.in).

Color versions of one or more of the figures in this paper are available online at http://ieeexplore.ieee.org.

when object diameter is comparable to the diameter of emitter/receiver. Large number of emitter-receiver pairs having small apertures can be used though lack of accessible physical space may impose constraints on the placement of associated circuitry. Budgetary requirement is also an important criterion for small scale setup development [7]–[9].

Arranging emitter-receiver pairs in a scanning array is an essential first step. Uniform configuration is preferred in almost every CT setup design for its inherent simplicity. It may however not be optimal in terms of the number and locations of the emitter-receiver pairs used. The associated costs may be high and also, a uniform configuration may fail to offer flexibility in altering sensors locations when desired. Use of non-uniform spacing between two consecutive emitters and their corresponding receivers has been explored earlier in various fields such as: (i) real time ultrasound process tomography for two-phase flow [9], (ii) probabilistic hybrid sensor fusion and optimization approach for aircraft composite components [10], (iii) ultrasonic sensor placement optimization in structural health monitoring using evolutionary strategy [11], (iv) efficient sensor placement optimization for securing large water distribution networks [12] and (v) two step optimization of transducer locations in single input single output tonal global active noise control in enclosures [13].

A. Motivation

The goal herein is to compare performances of uniform and non-uniform emitter-receiver pair arrangements for best tomographic reconstruction. One such study has been evaluated earlier [14]. Iterative search technique with the assumption of constant/smoothened projection data has been devised using 64 gamma ray detectors. To the best of our knowledge similar study is missing in literature that is related to non-destructive evaluation and CT using ultrasound modality. Location of emitter-receiver pairs around an object's (under investigation) periphery helps determine the chord length/path of an acoustic wave. A feedback loop between array designing and reconstruction process may prove favorable when (a) minimizing the cost of emitter-receiver pairs, (b) reducing path induced noise and (c) facilitating a uniform spread of information for better interpolation (explained in section 2). Setup design and a chosen reconstruction algorithm should be flexible enough to mutually exploit each others capabilities. This tomography inspired measurement setup design process is termed herein
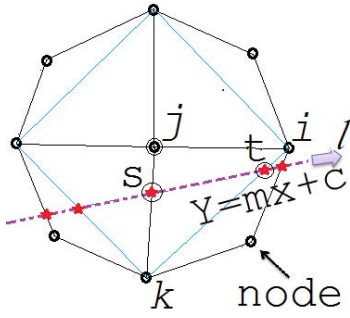
Fig. 1.   Example of discretization grid.

as "Tomometrics" and is discussed in the following section. Two scanning geometries (a) parallel and (b) fan beam are used with computer generated pixel images (cyber phantoms) and real world specimens. The best setup design is obtained and used to scan a batch case of water-gas flowing within a metal column. Commercially available numerical simulation tool FLUENT 14.0 [15] is used to simulate similar conditions for comparison. Finally, concluding remarks are made.

1) Tomometrics: Algebraic reconstruction algorithms are recommended options for limited detector and projection/view tomography (LDVT) problems [17]–[19]. Formulation of an iterative algorithm correlates real world projection data P_l as integrals along the path of an acoustic wave/ray emanating from the lth emitter towards its corresponding focused receiver. Line integral $\int f \, dl$ is interpreted as

$$\sum_{l=1, j=1}^{l \leq M, j \leq N} W_{lj} \cdot f_j = P_l. \qquad (1)$$

Here, f is the estimated nodal-density/void-fraction and *dl or its discrete approximation W* is the differential length. N and M are the number of nodes and total number of line integrals respectively. Structured Delaunay triangulation (DTS) grid (Fig. 1) is used for discretizing the image space. Weight coefficients are given via Eq. 2.

$$W_{lj} = \sum_{r=1}^{q} [\frac{\sqrt{(x_t - x_s)^2 + (y_t - y_s)^2}}{4A_{ijk}} \\ \times \{(y_k - y_i) + m_l (x_i - x_k)\} \\ \times (x_t - x_s) + (x_k y_i - x_i y_k) + c_l (x_i - x_k)] \qquad (2)$$

where q is the number of triangular elements each containing the jth node, l^{th} ray is the ray of projection passing through some of these triangles, and A_{ijk} is the area of the triangular element with nodes i, j and k. s and t are the intersection points of the lth ray and the triangular element ijk.

Parallel setup geometry is chosen, initially, for its inherent simplicity. A cylindrical object of diameter 168 mm is chosen to illustrate this study. Active diameter/aperture of emitter/receiver is considered as 12.5 mm. High wave frequency of 1 MHz is taken for better temporal and spatial resolution. Beam width or active diameter can be customized up to a desired chord length for focusing purpose before placing a purchase order [20]. Each wave/ray is assumed to
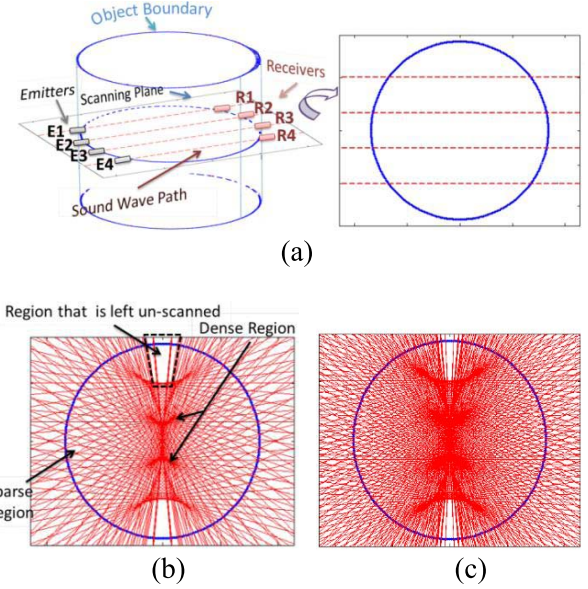

Fig. 2.   Spread of wave (line) for uniform configuration: irregularity in information spread increases with number of projections. (a) Single projection. (b) 36 projections. (c) 72 projections.

follow/replicate a focused path. A single scanning projection with 4 emitter-receiver pairs comprises of 4 such rays, as depicted via dotted lines in Fig. 2(a). Overall region swept by these rays (overlapped paths) represents part of the object's cross-section scanned.

Information that is gathered during scanning and utilized in recovery process belongs to the shaded area as depicted via the region of intersections between the dotted lines in Fig. 2. Scanning is allowed only within ±80 degrees due to presence of pressure transducers (Figs. 7 and 8) and other associated circuitry. This area is characterized by dense and sparse regions. Vacant, un-scanned parts of the cross-section (white region in Fig. 2) can be termed as zero information regions. It is shown in Fig. 2(b) that *non-uniform radiation spread exists for particular scanning constraints. An* iterative reconstruction algorithm distributes the energy content of projection data in a pixelated image. There can be three kinds of pixels in a reconstruction grid: (a) a pixel that has been crossed by more number of rays (in the dense region), (b) a pixel that has been crossed by comparatively few numbers of rays (belonging to the sparse area) and finally (c) a pixel with no rays. Undesirable, unmapped inactive pixels in last category relate to zero weight coefficients for all projections [17]. It is shown in Figures (1) and (2) via analytical expression in Eq. (2) that *information spread* and weight coefficients depend on wave path/ray geometry/line-of-sight and thus are implicitly decided by the arrangement of emitter-receiver pairs. Pixels in denser region, thus, have high probability to participate in recovery process. Variation of this information spread can be minimized by adjusting the locations of these emitter-receiver pairs. *This can be formulated by (a) decreasing the normalized variance of the weight matrix and (b) optimally smear/mask the estimated information.*

The area of the zero information regions can be minimized by scanning with more number of angles with finer intervals.

Region left un-scanned shrinks with 72 projections (Fig. 2c). Information distribution, however, appears denser at central region in comparison to 36 projections case. This case (72 projections) is not considered for further analysis because (a) non-uniformity in information spread increases, (b) scanning time increases [21], [22] and (c) compact devices require costly and sophisticated installations. *Such cases motivate us to place emitter-receiver pairs in a specific optimal fashion (non-uniform configuration) that would minimize/normalize the occurrence of dense, sparse and un-scanned regions by achieving a uniform spread of information.*

Configuration that provides reconstruction with least root mean square error and a coefficient weight matrix having low variance is considered optimal. This hypothesis is tested using noise free synthetic projection data that is obtained from a computer generated cyber image/phantom. Constraints are (a) minimum spacing between two consecutive emitters/receivers, (b) boundary conditions, e.g., acoustic beams must remain inside of object/pipe and (c) ratio of the object diameter to emitter/receiver diameter. These conditions permit a maximum of 4 emitter-receiver pairs (to be placed optimally) with considered setup specifications (details in section 2) in our case.

II. Estimation of a Non-Uniform Emitter-Receiver Pair Configuration

Acoustic waves must propagate inside an object's periphery. Emitters/receivers are therefore constrained to remain 10 mm (more than half of the beam width) inside the inner boundary of the object/pipe. Minimum permitted distance of 20 mm is kept fixed between two consecutive emitter-receiver pairs for holding purpose. Genetic algorithm (GA) is used to evolve the possible arrangements of emitter-receiver pairs. Inbuilt function *gaTool* in the MATLAB optimization toolbox is used for implementation [23]. Fitness function is scaled via the rank selection mode. Default settings in this toolbox are used.

This toolbox is coupled with another code that performs tomographic reconstruction. Modified entropy maximization algorithm (sMaxenT) is used for reconstruction [17], [18], [24]. It utilizes entropy function to estimate optimized smearing/filtering parameters in each iteration. Implementation details of entropy optimization technique are discussed elsewhere [17], [18]. Usually, number of pixels in the reconstruction grid is taken equal to number of emitter-receiver pairs. We cannot expect a meaningful reconstruction in our case (image with 4 pixels only) [17], [25]. Number of pixels/nodes is, therefore, also incorporated within optimization loop. Structured Delaunay triangulation (DTS) grid is used for reconstruction. Optimization variables are (a) locations of emitter-receiver pairs, (b) variance of normalized weight matrix and (c) number of pixels in the reconstruction grid.

III. Simulation

Simulation study is performed with two computer generated images (Phantom1 in Fig. 3(a) and Phantom2 in Fig. 6(c)). Projection data is generated for 40×40 nodes (Fig. 3(a))
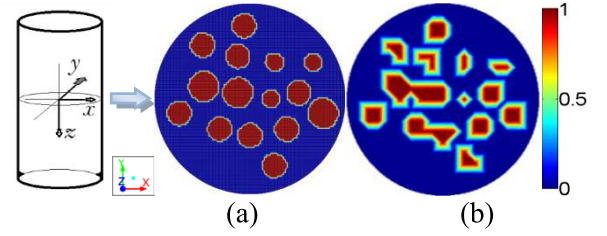

Fig. 3. Depiction of Phantom1. (a) Phantom1 (40 pixels). (b) Phantom1 (18 pixels).

TABLE I
DETAILS OF DESIGN

Arrangement		Optimal	Uniform
Emitter-receiver pair location#	D1	-65.00	-50.40
	D2	-07.40	-16.80
	D3	+26.50	+16.80
	D4	+75.50	+50.40
Error		0.039	0.171
Focal length		514.0	602.0
Reconstructed AA*		0.153	0.157

Distance from center (in mm); *Area Average or mean of function value.

to garner sufficient information. Phantom1 represents a two dimensional (2D) cross-section of a two phase flow channel at a certain height. Choice of a binary color scheme is equivalent to any two phase flow case. Red depicts higher acoustic impedance, for example, gas phase fraction. Significant fraction of air (70%) is distributed within 0.7 of the object/pipe radius. This prior information is deduced according to the sparger design [30].

Finally, the formulation converges on (a) 18×18 pixels and (b) a non-uniform arrangement of emitter-receiver pairs, for this phantom. Cyber image (area average 0.15), equivalent to this grid resolution is shown in Fig. 3(b). Reconstruction details are given in Table I and images are shown in Fig. 4.

Optimal formulation provides non-uniform locations in contrast to the usual understanding. Emitter-receiver pairs termed as E1R1 and E4R4 appear much nearer to the object boundary in the non-uniform arrangement (Fig. 4(d)). The zero information regions (unshaded portion within the circle) are reduced in area compared to the uniform arrangement (Figures 4(b) & 4(e)). These zero information regions cannot be removed entirely due to the boundary conditions used (the emitter-receiver pairs must remain inside 10 mm from inner boundary). It is observed that the third ray path, E3R3, evolves much nearer to the center (7.4 mm below in Fig. 4(d)) compared to the uniform configuration (16.8 mm below in Fig. 4(a)). Third conic lobe from top down (Fig. 4(b)) is pushed deep back towards the center (Fig. 4(e)) due to this arrangement. It is confirmed that optimized locations are helpful in achieving a more uniform spread of information across the object's cross-section. Total focal length for the optimized emitter-receiver pairs arrangement case (E1R1 + E2R2 + E3R3 + E4R4) is 514 mm (minimum is 86 mm for E1R1 and maximum is 166 mm for E3R3). The same is 602 mm (minimum is 135 mm for E1R1 and maximum
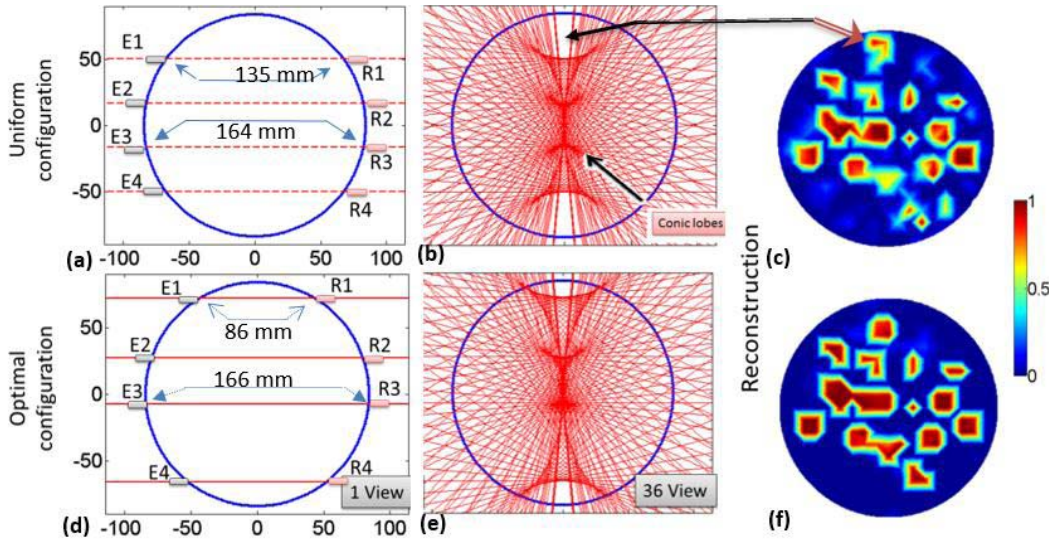
Fig. 4. Ray spread for optimized emitter-receiver pairs alignment: area that is left un-scanned is less and rays are gradually distributed than in uniform configuration case. (a) and (d) Single projection. (b) and (e) 36 projections.

is 164 mm for E3R3/E2R2) for the uniform configuration. This is depicted in Figures 4(a) and 4(d). This adjustment reduces the setup budget and the emitter-receiver pair (with smallest focal length) exchanges less diverging beam with sufficient energy component. Variances of weight matrix are 1.3×10^{-5} and 1.1×10^{-5} for uniform and optimized configurations respectively.

Reconstruction results corresponding to uniform and optimized emitter-receiver pair locations are shown in Figures 4(c) and 4(f) respectively. It is observed that reconstruction in case of the uniform emitter-receiver pairs arrangement (Fig. 4(c)) fails to recover the true density values and shapes corresponding to zero information regions. Reconstruction result for the optimized locations (Fig. 4(f)), however, recovers all shapes successfully but fails to recover precise density values at the corresponding locations. Real data measurements are performed next.

IV. ANALYSIS WITH REAL DATA

Following two assemblies (fan and parallel beam) are commissioned for testing the proposed concept with objective of void fraction measurements. Details are provided below.

A. Setup Details for Parallel Beam Geometry

Tomography setup with two (uniform and optimized) configurations is developed in-house. Interface between hardware (Fig. 5(a)) and software is achieved via LabVIEW software package. A stainless steel frame/casing with perspex holder (shown in Fig. 5(a), inset, left bottom) is established. Choice of steel frame is justified due to its prolific use in industries, e.g., oil, fracking, pharmaceutical etc. Propagation time of waves, which are not traveling via area of interest, remains fairly constant. Waves via pipe/frame boundary are filtered out to extract meaningful signal (Fig. 5(b)) [26]. Integrated virtual instrument and toolbox in LabView and MATLAB are used for signal processing [23], [27], [28].

Specimen1, (Fig. 6(a)) is used to validate the optimal location hypothesis for this parallel beam setup. It is made of
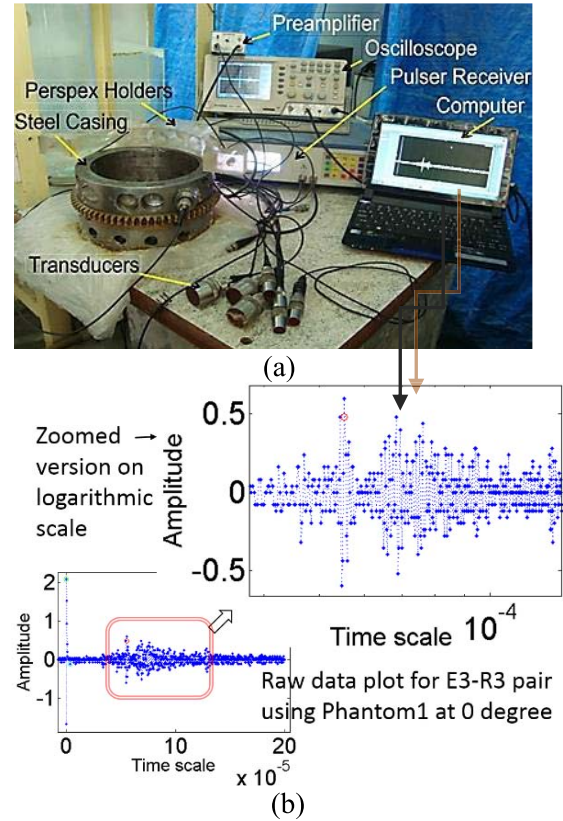

Fig. 5. Experimental setup. (a) Setup. (b) Acoustic waveform.

7 steel rods (5 rods of 12 mm and 2 rods of 8 mm diameter) fixed on a perspex base. Surrounding fluid is water. Line-of-sight at the height of scanning, where emitter-receiver pairs are fixed, swaps all 7 rods and water (Fig. 6(b)). Perspex is used for holding these rods and it does not belong to the area of interest. Top view of this specimen (Fig. 6(d)) is shown for visual comparison. Specimen1 is rotated manually for 36 projections (5^0 each).
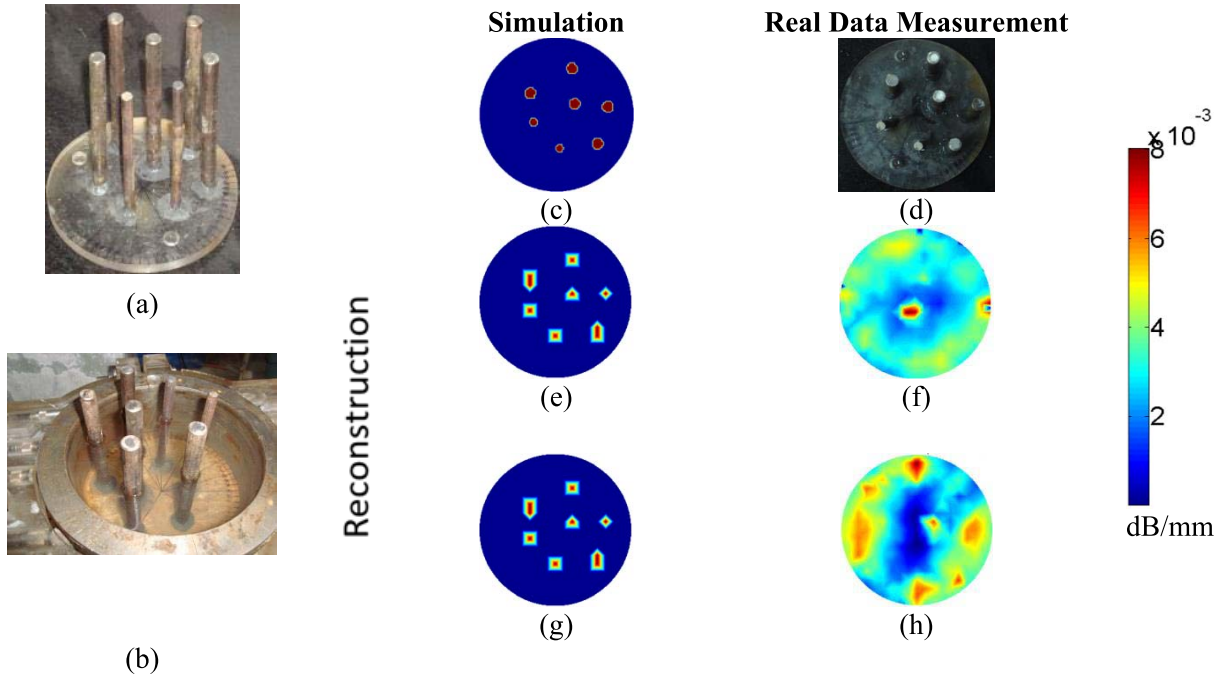
Fig. 6.   Setup characterization and reconstruction of real data: reconstruction result of optimized location case is able to recover the relative locations of 7 rods. (a) Specimen1. (b) Inside the frame with water. (c) Phantom2. (d) Top view of Specimen1. (e) and (f) Uniform configuration. (g) and (h) Non-uniform configuration.

Angular displacement for each rotation $\pi \times 168/2/180 = 1.4$ *mm* is 0.87% of the object's diameter. The error for the center of rotation is considered negligible. Average of 40 readings per projection per emitter-receiver pair is saved to subdue any uncertainty in measurements. Error estimates are not available for limited data problem [17], [22]. Next best alternative is to examine the performance of the setup by scanning and reconstructing a real world Specimen1 (Figures 6(a), 6(b) and 6(d)) with a known inner design. Computer generated image of Specimen1 (Phantom2) is shown in Fig. 6(c). Synthetic projection data is also generated from this image. Standard acoustic impedance values are used [29]. Reconstructions of Phantom2 using this data are shown in Figures 6(e) and 6(g). Both uniform and non uniform configurations perform equally well with insignificant difference. We note that variations in inner profile is small corresponding to zero information regions. Signal to noise ratios (20.67 dB for non-uniform and 11 dB for uniform case) are estimated by normalized synthetic (noise free) and measured projection data for estimating the level of noise during data collection.

Reconstructed cross-sections of Specimen1 using real time measurements are shown in Figures 6(f) and 6(h) for uniform and optimized configurations respectively. Details of analysis are provided in Table II.

Location of rods w.r.t. the base seems inflated/zoomed hence displaced w.r.t. specimen boundary but their relative positions are preserved during the tomographic recovery process. Contrast resolution between steel rods and water is sufficient to distinguish the difference between various boundaries. Difference due to configuration is pronounced in case of real data measurements.

TABLE II
DETAILS OF RECONSTRUCTION

Configuration		Uniform	Non-uniform
Cyber replica	AA	2.09×10^{-4}	2.08×10^{-4}
	Max_f	0.008	0.008
	RMSE	0.300	0.294
Real	AA	0.0037	0.003
	Max_f	0.0074	0.0085

Holistic performance of the non-uniform case appears promising compared to the uniform configuration. It is observed that using only 4 emitter-receiver pairs with 36 projections, Fig. 6(h) is the best reconstruction that can be achieved by this UCT setup.

B. Setup Details for Fan Beam Geometry

Emitter-receiver pairs are mounted on a fluid flow channel by a steel frame in the Perspex holder. Steel is preferred for a strong automatic/mechanized rotating (computer controlled) frame for faster data acquisition. It is found that due to multiple interfaces, focused parallel beam diverges. Emitter and receiver apertures are not always perpendicular to the object periphery in parallel beam mode, leaving a gap between the object and the emitter/receiver surface. We believe such interfaces, however, filled with coupling medium, corrupt the useful acoustic signal. Failed design is shown in Fig. 7(a). Loss of direct contact is unavoidable in parallel beam mode.
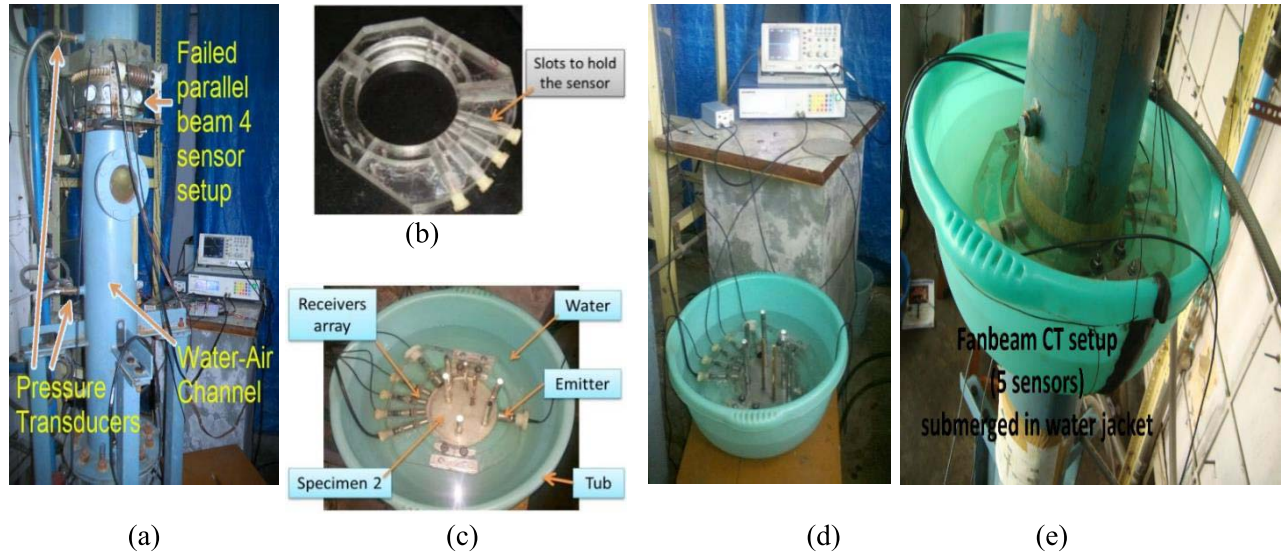
Fig. 7.   Experiment with optimized emitter-receiver array design. (a) Parallel beam setup on water channel. (b) Fan beam non-uniform *optimized* design. (c) Specimen2 submerged in water tub. (d) Calibration with Specimen2. (e) Void fraction measurement setup on fluid channel.
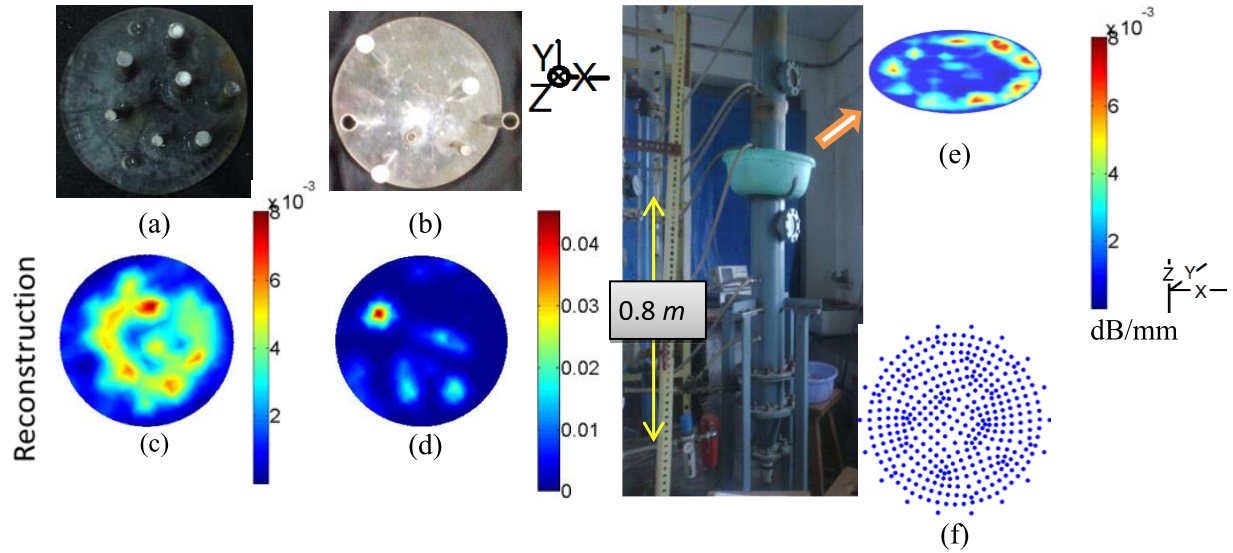

Fig. 8.   Calibration and characterization of the algorithm using fan beam arrangement. (a) Specimen1. (b) Specimen2. (c) Reconstruction of Specimen1. (d) Reconstruction of Specimen2. (e) Reconstructed image of pure water in air-water channel. (f) Grid.

A new array (5 receivers and single emitter) is designed in fan beam mode to cope with this drawback. Odd number of receivers are taken to avoid absence of focused wave/ray in the central chord. Similar Tomometrics approach (as discussed earlier in Section 4) is used for this fan beam array design. Design with non-uniform emitter-receiver pairs arrangement is used to measure void-fraction across the steel pipe. Perspex holder with non-uniform slots is shown in Fig 7(b). It is mounted directly, i.e., without the aid of a steel frame. Specimen1 and Specimen2 (details follow) are used to test/calibrate this setup before they are mounted on metal pipe at the height of 0.8 m from the sparger.

An ingenious arrangement is achieved/tested by creating a water jacket (Figures 7(c), 7(d) and 7(e)). Water envelope provides an efficient coupling environment. An automatic

mechanism can also be designed. Measurement setup arrangements for (a) calibration and (b) void-fraction measurement are shown in Figures 7(c), 7(d) and 7(e). Water-air channel or bubble column is a part of multi-phase flow system created in the laboratory environment [30]. Calibration is performed to (a) verify the setup's circuitry (developed in-house), (b) validate the signal processing step and (c) estimate the normalization factor between the reconstruction code's color scale and real world attenuation coefficient.

Specimen1 (Fig. 8(a)) and Specimen2 (Fig. 8(b)) are used for this purpose. Specimen2 is made of 7 hollow metal tubes. Two tubes are made of copper metal having 0.7 cm diameter and other five are made of steel with 1.2 cm diameter. Four of these tubes (including one copper tube) are filled with fine glass beads (average size of 35 μm) [30]. This material

TABLE III

NORMALIZATION FACTOR CALCULATION

Material	SS304	Water
Standard	0.0531	2.2×10^{-4}
Recovered	0.0083	3.75×10^{-5}
Normalization Factor	6.3	5.9

mimics slurry/sand particles. Table III contains standard and recovered acoustic attenuation coefficients (dB/mm) [31], [32]. Measured acoustic attenuation coefficients of iron and water are estimated from maximum and minimum recovered values in reconstruction of Specimen1. Comparison of these values reveals that the normalization factor is approximately equal to 6 in both cases.

Reconstructed images for Specimen1 and Specimen2 are shown in Figures 8(c) and 8(d) respectively. Top views (for sake of visual comparison) of corresponding specimens are shown in Figures 8(a) and 8(b). It is observed that despite the change in number of emitter-receiver pairs and their arrangement, color scales of reconstructed images of Specimen1 (Figures 6 and 8) are almost similar. Reconstruction quality however ($r.m.s.e = 21\%$ compared to 36% in 4 emitter-receiver design earlier), is improved. Depiction of iron rods is still diffused but their respective locations w.r.t. each other and w.r.t. the circular boundary are nearly the same as original. Reconstruction for Specimen2 is shown in Fig. 8(d). Algorithm fails to accurately distinguish the profile of tubes with glass beads. We note that distribution of glass beads (inside tubes) also contains non-uniform air cavities.

Experiments are performed on air-water channel at 0.80 m height. Dynamic bias error assumed to has negligible effects over CT image reconstructions [22]. Scanning is first performed on pure water filled channel (static water). Setup is shown in Fig. 7(e). Whole pipe (1.60 m) is discretized in unstructured hexahedral 3D meshes using open source Gambit meshing tool.

Discretization grid used for CT reconstructions of flow measurements is shown in Fig. 8(f). Effect of discretization grids with employed iterative reconstruction algorithm has been studied extensively for variations in grid dependent parameters. This analysis (excluded for brevity) shows negligible deviations. Boundary of metal pipe (Fig. 8(e)) is recovered with negligible artifacts but periphery has unsymmetrical depiction. It is because thickness of this pipe/channel is not uniform. The reconstruction algorithm is able to recover metal pipe as well as static water content with considerable contrast resolution. Maximum recovered acoustic impedance (i.e., steel) in this case is the same as it is recovered in earlier sections.

C. Void-Fraction Measurement

Non-invasive imaging of a two phase flow channel is presented next to justify the real world application of this study. Air flow inside a static water column is investigated. Setup is mounted on a fixed column and rotated manually to avoid any vibration. Measurements for air-water distribution are

performed for five different air flow rates of 400, 500, 600, 700 and 800 cc/sec. Water is kept static for all 5 batch cases. Few such conditions exist in medical, chemical and oil industries [6], [30], [34]. Amount of air restricts the transmission of ultrasound waves between an emitter and the corresponding receiver. It becomes difficult to extract useful signal from the background signals beyond 800 cc/sec using the employed signal processing technique. This limiting point decides the maximum flow rate that can be measured by this setup.

Numerical simulation (3D) is performed using commercially an available tool FLUENT 14.0 [15]. Approximately 10% of the inlet has been treated as blockage to model the sparger. Virtual mass force and forces due to change in viscosity are neglected. A proper initial guess is required in numerical simulation otherwise iterations may diverge. Simulation is performed in two stages: (a) a mixture model is used in the first stage and (b) converged phase fraction values (outcome of the mixture model) are used as an initial guess with multiphase Eulerian model. Two drag force modification laws (a) Tomiyama and (b) Schiller-Naumann are used for comparative modelling [33]. Reconstructed air phase fraction CT profiles and 3D simulated profiles (Tomiyama drag law) are shown in Fig. 9 for all five flow rates.

All images are shown on the same normalized scale. It is inferred that air distributions, obtained by the CT approach, grow around a smooth annular region with few discrete high contrast spots. Distributions, obtained by FLUENT, also have similar but comparatively smoother patterns. Occurrence of discrete spots increases with air flow rates in CT images. This indicates sensitivity of measurements to detect the presence of air bubbles. Inner diameter of ring/annular region contracts with flow rate. This observation is in accord with the usual air-water interaction. Details of these results are provided in Table IV. Numerical simulation results for 400, 500 and 600 cc/sec show similar characteristics. Estimated phase fraction values by Tomiyama model (maximum relative deviation −24.6 %) are in better agreement compared to the Schiller-Naumann model (maximum relative −52.0 %). Air phase fraction values by numerical simulations are assumed as standard in this calculation. It is observed that simulated air fraction increases almost linearly for Schiller-Naumann and Tomiyama models but having different slopes. Finally, air phase fractions (mean of air fraction) by CT and numerically simulated techniques (Tomiyama and Schiller-Naumann) are plotted in Fig. 10. Measured air fractions (CT) are slightly larger than estimated values (FLUENT) for 400, 500 and 600 cc/sec air flow rates. Results by the CT and Tomiyama drag law are comparable for air flow rate of 700 cc/sec. Air phase fraction by CT is less than the simulated estimation for 800 cc/sec. Perfect drag laws are still under development. These results are in accord with a previously reported work [30].

V. DISCUSSION

Optimal design (arrangement of emitter-receiver pairs) depends on inner profile because l_2 norm/function value is incorporated in the optimization formulation. We report that
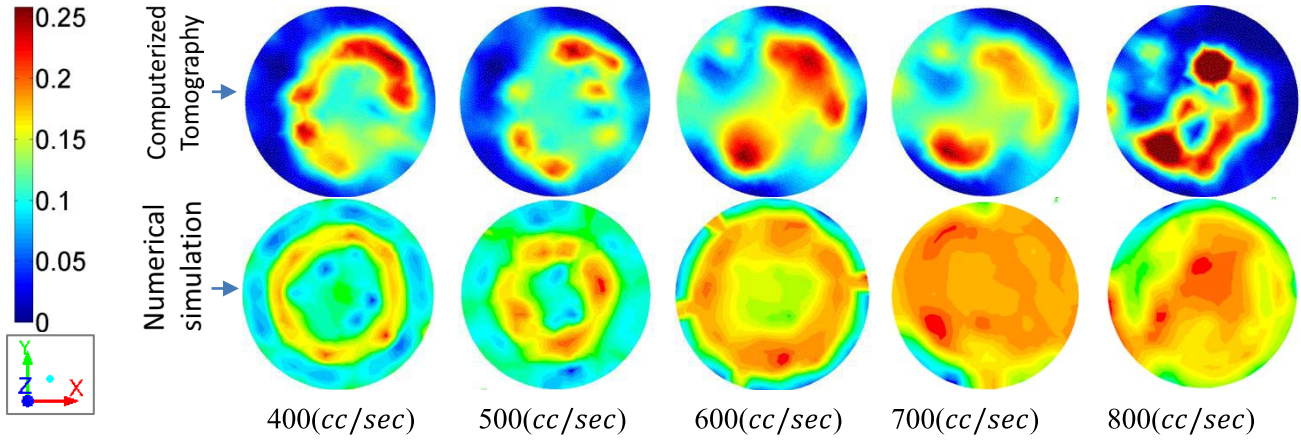
Fig. 9. Air distribution (CT reconstructed and numerically simulated images): Air flows towards center with increase in air flow rates, CT reconstructions contain less uniform distribution of air.

TABLE IV
DETAILS OF AIR PHASE FRACTION PROFILES

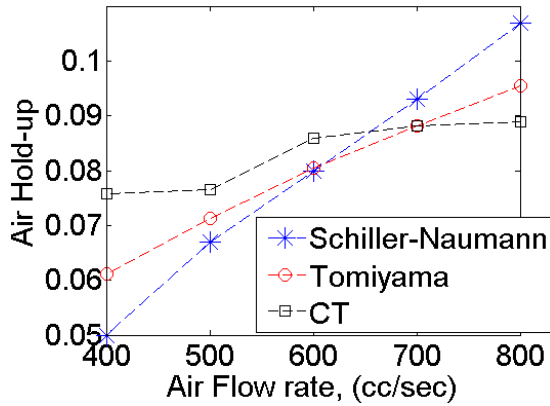| Air volume flow rate w.r.t. water (cc/sec)	Fraction				
	Measured	Simulated (Eulerian Model)			
	CT	Tomiyama	Deviation %	Schiller–Naumann	Deviation %
400	0.076	0.061	-24.59	0.050	-52.00
500	0.078	0.071	-09.89	0.067	-16.41
600	0.086	0.080	-07.50	0.080	-07.50
700	0.088	0.088	00.00	0.093	05.37
800	0.089	0.095	06.31	0.107	16.82

Fig. 10. Air phase fraction: CT and simulation provide results in similar range.

the optimal design for Specimen1 is slightly different from that for Phantom1. Capability to drill the slots for another profile specific holder with these slight differences is also a necessity. An on-spot amorphous setup design can be created to utilize this analysis that would change/adjust (a) the arrangement of emitter-receiver pairs, (b) setup geometry parameters (distances between emitter, receiver and object) and (c) fan angle, via a feedback loop. This would help in obtaining better reconstructions but may put constraints on budget optimization. The approximate profile reconstructed by the uniform emitter-

receiver pairs arrangement can also be used in the first stage for optimized emitter-receiver pairs configuration. It is possible to create a profile independent arrangement of emitter-receiver by using the variance of weight matrix as a primary criterion. Prior information may or may not be needed (such as sparger design) for more accurate exploitation of the proposed scanning strategy. Adaptive grid, as an alternative, provides better reconstruction where information distribution is non-uniform. These discussions are beyond the scope of this work.

VI. CONCLUDING REMARKS

Following findings are reported in this work:

1) Optimal and uniform emitter-receiver alignments are compared for ultrasound computerized tomography. Simulation and real data analysis indicate that optimal alignment provides better way of scanning as far as tomography reconstructions of a sparse data is concerned.

2) Optimal setup design facilitates reconstructions just using few emitter-receiver pairs.

3) It is also shown that the required focal lengths of emitter-receiver pairs are less for the optimal configuration than in uniform case. It is assumed that cost of an emitter/receiver is proportional to its focal length. Optimal design is, therefore, helpful in reducing the expenditure before emitter/receiver pair purchase. It is $\frac{514-602}{602} \times 100 = 14.6\%$ less when emitter-receiver

pairs are placed at optimal locations (in parallel beam case).

4) Void fraction measurement is performed to demonstrate a real life application. Reconstructed air phase fractions (distribution and fraction) are successfully compared with numerical simulated results obtained by FLUENT 14.0.

We now recommend that such tomometric exercises can be beneficial to achieve better limited data tomography reconstruction.

REFERENCES

[1] S. Chakraborty, E. Keller, J. Talley, A. Srivastav, A. Ray, and S. Kim, "Void fraction measurement in two-phase flow processes via symbolic dynamic filtering of ultrasonic signals," *Meas. Sci. Technol.*, vol. 20, no. 2, p. 023001, 2009.

[2] M. H. F. Rahiman, R. A. Rahim, M. H. F. Rahiman, and M. Tajjudin, "Ultrasonic transmission-mode tomography imaging for liquid/gas two-phase flow," *IEEE Sensors J.*, vol. 6, no. 6, pp. 1706–1715, Dec. 2006.

[3] A. A. Samokrutov and V. G. Shevaldykin, "Ultrasonic tomography of metal structures using the digitally focused antenna array method," *Russian J. Nondestruct. Test.*, vol. 47, no. 1, pp. 16–29, 2011.

[4] Y. Xu, L. V. Wanga, G. Ambartsoumian, and P. Kuchment, "Reconstructions in limited-view thermoacoustic tomography," *Med. Phys.*, vol. 31, no. 4, pp. 724–733, 2004.

[5] M. Krueger, V. Burow, K. M. Hiltawsky, and H. Ermert, "Limited angle ultrasonic transmission tomography of the compressed female breast," in *Proc. IEEE Ultrason. Symp.*, Oct. 5–8, 1998, pp. 1345–1348.

[6] L. Büttner *et al.*, "Dual-plane ultrasound flow measurements in liquid metals," *Meas. Sci. Technol.*, vol. 24, no. 5, pp. 055302-1–055302-12, 2013.

[7] H.-Y. Tseng, "Welding parameters optimization for economic design using neural approximation and genetic algorithm," *Int. J. Adv. Manuf. Technol.*, vol. 27, nos. 9–10, pp. 897–901, 2006.

[8] G. Roehrlein and H. Ermert, "Limited angle reflection mode computerized tomography," in *Acoustical Imaging*, vol. 14. New York, NY, USA: Plenum, 1985.

[9] M. Yang, H. I. Schlaberg, B. S. Hoyle, M. S. Beck, and C. Lenn, "Real-time ultrasound process tomography for two-phase flow imaging using a reduced number of transducers," *IEEE Trans. Ultrason., Ferroelectr., Freq. Control*, vol. 46, no. 3, pp. 492–501, May 1999.

[10] S. Costiner *et al.*, "A probabilistic hybrid sensor fusion and optimization approach for aircraft composite components," *J. Intell. Mater. Syst. Struct.*, vol. 24, no. 17, pp. 2110–2134, 2013.

[11] H. Gao and J. L. Rose, "Ultrasonic sensor placement optimization in structural health monitoring using evolutionary strategy," in *Proc. AIP Conf., Rev. Quant. Non-Destruct. Eval.*, vol. 820, 2006, pp. 1687–1693.

[12] A. Krause, J. Leskovec, C. Guestrin, J. VanBriesen, and C. Faloutsos, "Efficient sensor placement optimization for securing large water distribution networks," *J. Water Resour. Planning Manage.*, vol. 134, no. 6, pp. 516–526, 2008.

[13] J. I. Palacios, J. Romeu, and A. Balastegui, "Two step optimization of transducer locations in single input single output tonal global active noise control in enclosures," *J. Vibrat. Acoust.*, vol. 132, no. 6, pp. 061011-1–061011-8, 2010.

[14] M. Yamamoto, "Detector arrangement and sampling characteristics in rotary positron-emission computed tomography," *Phys. Med. Biol.*, vol. 26, no. 3, p. 489, 1981.

[15] *ANSYS Fluent14.0 Theory Guide*, Cecil Township, PA, USA, 2014.

[16] Y. Arai, E. Tammisalo, K. Iwai, K. Hashimoto, and K. Shinoda, "Development of a compact computed tomographic apparatus for dental use," *Dentomaxillofacial Radiol.*, vol. 28, no. 4, pp. 245–248, Jul. 1999.

[17] M. Goswami, A. Saxena, and P. Munshi, "A new grid-based tomographic method for two-phase flow measurements," *Nucl. Sci. Eng.*, vol. 176, no. 2, pp. 240–253, 2014.

[18] M. Goswami, P. Munshi, A. Saxena, M. Kumar, and A. Kumar, "Plasma diagnostics at Aditya Tokamak by two views visible light tomography," *Fusion Eng. Design*, vol. 89, no. 11, pp. 2659–2665, Nov. 2014.

[19] S. K. Rathore, N. N. Kishore, and P. Munshi, "An improved method for ray tracing through curved in homogeneities in composite materials," *J. Nondestruct. Eval.*, vol. 22, no. 1, pp. 1–9, Mar. 2003.

[20] [Online]. Available: http://www.ultrangroup.com/index.php/products/transducers/non-contact/line-cylindrical-foused/, accessed Feb. 2012.

[21] D. O. Trad, T. J. Ulrych, and M. D. Sacchi, "Accurate interpolation with high-resolution time-variant radon transforms," *Geophysics*, vol. 67, no. 2, pp. 644–656, Mar. 2002.

[22] S. Shakya, P. Munshi, M. Behling, A. Luke, and D. Mewes, "Analysis of dynamic bias error in X-ray tomographic reconstructions of a three-phase flow system," *Int. J. Multiphase Flow*, vol. 58, pp. 57–71, Jan. 2014.

[23] [Online]. Available: http://www.mathworks.com/MATLAB7.8.0 (R2009a)

[24] E. G. Bazulin, "Reconstruction of the images of reflectors from ultrasonic echo signals using the maximum-entropy method," *Russian J. Nondestruct. Test.*, vol. 49, no. 1, pp. 26–48, 2013.

[25] Z.-C. Lin and G. Wade, "On the resolution of planar ultrasonic tomography," *J. Acoust. Soc. Amer.*, vol. 77, no. 1, p. 139, 1985.

[26] J. Kim, L. Udpa, and S. Udpa, "Multi-stage adaptive noise cancellation for ultrasonic NDE," *NDT & E Int.*, vol. 34, no. 5, pp. 319–328, 2001.

[27] [Online]. Available: http://www.signal.uu.se/Toolbox/USPT/

[28] [Online]. Available: http://www.mathworks.in/matlabcentral/fileexchange/28367-the-lamb-toolbox

[29] T. P. Lerch and S. P. Neal, "Attenuation coefficient estimation using equivalent diffraction points with multiple interface reflections," in *Proc. AIP Conf., Rev. Quant. Nondestruct. Eval.*, vol. 22, 2003, p. 657.

[30] S. Kumar, N. Srinivasulu, P. Munshi, and A. Khanna, "Flow regime transition identification in three phase co-current bubble columns," *Can. J. Chem. Eng.*, vol. 91, no. 3, pp. 516–523, 2013.

[31] A. Vladišauskas and L. Jakevičius, "Absorption of ultrasonic waves in air," *Ultragarsas*, vol. 50, no. 1, p. 50, 2004.

[32] C.-H. Hsu, H.-Y. Teng, and S.-C. Chiu, "Ultrasonic evaluation of temper-embrittlement for martensitic stainless steel," *Mater. Trans.*, vol. 44, no. 11, pp. 2363–2368, 2003.

[33] H.-P. Luo and M.-H. Al-Dahhan, "Verification and validation of CFD simulations for local flow dynamics in a draft tube airlift bioreactor," *Chem. Eng. Sci.*, vol. 66, no. 5, pp. 907–923, 2011.

[34] D. K. Swanson *et al.*, "Arterial blood flow measurement using digital subtraction angiography (DSA)," *Proc. SPIE, Med. Imag. Instrum.*, vol. 486, p. 122, Aug. 1984.

Mayank Goswami received the B.E. degree in electrical engineering from the Madhav Institute of Technology and Science, Gwalior, India, in 2006, and the M.Tech. and Ph.D. degrees in nuclear engineering and technology program from the Indian Institute of Technology Kanpur, Kanpur, India, in 2009 and 2014, respectively. His research interests are the development of compact CT setups, signal processing techniques, and reconstruction algorithms for sparse data inverse problems.

Prabhat Munshi is currently a Professor with the Department of Mechanical Engineering, Indian Institute of Technology Kanpur, Kanpur, India. He received the B.Tech. degree in mechanical engineering from the Indian Institute of Technology Kanpur, in 1977, the M.S. degree in nuclear engineering from Ohio State University, Columbus, OH, USA, in 1979, and the Ph.D. degree in nuclear engineering and technology program from the Indian Institute of Technology Kanpur, in 1989. His research interests are computerized tomography, nondestructive testing, and evaluation nuclear safety analysis and multiphase flow measurement.

Ashok Khanna is currently a Professor with the Department of Chemical Engineering, Indian Institute of Technology Kanpur, Kanpur, India, where he received the B.Tech., M.Tech., and Ph.D. degrees in chemical engineering in 1969, 1972, and 1989, respectively. His areas of interest include multiphase flows, process control, and separation process.

Anupam Saxena is currently an Associate Professor with the Department of Mechanical Engineering, Indian Institute of Technology Kanpur, Kanpur, India. He received the B.Tech. degree from the Indian Institute of Technology Bombay, Mumbai, India, in 1995, the M.S. degree from the University of Toledo, Toledo, OH, USA, in 1997, and the Ph.D. degree in mechanical engineering from the University of Pennsylvania, Philadelphia, PA, USA, in 2000. His research interests pertain to compliant and robotics systems.